Merging Boron and Carbonyl based MR-TADF Emitter Designs to Achieve High Performance Deep Blue OLEDs

Sen Wu,[a] Le Zhang,[a,b] Jingxiang Wang,[a] Abhishek Kumar Gupta,[a] Ifor D. W. Samuel[b] and Eli Zysman-Colman[a]**

[a]Organic Semiconductor Centre, EaStCHEM School of Chemistry, University of St Andrews, St Andrews, Fife, UK, KY16 9ST, Fax: +44-1334 463808; Tel: +44-1334 463826; E-mail: eli.zysman-colman@st-andrews.ac.uk.

[b]Organic Semiconductor Centre, SUPA School of Physics and Astronomy, University of St Andrews, St Andrews, UK, KY16 9SS.

Abstract

Multiresonant thermally activated delayed fluorescence (MR-TADF) compounds are attractive as emitters for organic light-emitting diodes (OLEDs) as they simultaneously can harvest both singlet and triplet excitons to produce light and show very narrowband emission, which translates to excellent colour purity. Here, we report the first example of a MR-TADF emitter (**DOBDiKTa**) that fuses together fragments from the two major classes of MR-TADF compounds, those containing boron and those containing carbonyl groups as acceptor fragments in the polycyclic aromatic hydrocarbon skeleton. Using this molecular design, this compound shows desirable narrowband deep blue emission and efficient TADF character. The OLED with **DOBDiKTa** as the emitter and mCP:PPT (1:1) as the co-host exhibits an EQE_{max} of 17.4%, an efficiency roll-off of 32% at 100 cd m^{-2}, and CIE coordinates of (0.14, 0.12). Compared to **DOBNA** and **DiTKa**, **DOBDiKTa** shows higher device efficiency with reduced efficiency roll-off while maintaining a narrow pure blue electroluminescence, which demonstrates the promise of the proposed molecular design.

Thermally active delayed fluorescence (TADF) materials show great potential as emitters in the organic light-emitting diodes (OLEDs),[1–3] due to their capacity to harvest both singlet and triplet excitons and convert these into light. This is possible as a result of fast reverse intersystem crossing (RISC), which can occur in systems with small singlet-triplet energy gaps (ΔE_{ST})[4,5] and outcompetes non-radiative decay pathways. In traditional donor-acceptor TADF compounds, the small ΔE_{ST} results from the small exchange integral of the frontier orbitals that is possible in strongly twisted conformations where the donor and acceptor are mostly electronically decoupled.[6] A consequence of this molecular design that leads to long-range

charge transfer (LRCT) excited states is that the emission spectrum is broad, characterized by a full width at half maximum (FWHM) larger than 70 nm.[7] Thus, OLEDs using D-A TADF emitters typically show poor color purity. Notably, to obtain the blue electroluminescence (EL) that can meet the BT.2020 standard, *i.e.,* CIEy $\leqslant$ 0.05, without significant loss of efficiency caused by the use of color filters or microcavities will require the use of narrowband emitters.[8,9]

In 2016, Hatakeyama and co-workers reported the first examples of boron-based multiresonant TADF (MR-TADF) emitters, which showed simultaneously high photoluminescence quantum yields (Φ_{PL}), sufficiently small ΔE_{ST}, and narrowband blue emission (FWHM of 28 nm).[10] This seminal work has catalyzed significant efforts towards the development of boron-containing analogs, and also led to the expansion of the chemical space of MR-TADF emitters towards derivatives with the p-dopant replaced by carbonyl moieties.[11–13] The oxygen-bridged boron-contained MR-TADF emitter DABOA (2a) was the first p-, and n-doped polycyclic aromatic hydrocarbon reported by Hatakeyama.[14,15] This compound shows near-UV narrow emission, with a λ_{PL} of 398 nm and a FWHM of 34 nm in toluene solution.[15–17] Since this first report in 2015, many derivatives of DABOA (aka **DOBNA**) have been reported, where DOBNA frequently takes the role of a weak acceptor in donor-acceptor TADF emitters. In 2019, both Liao's group and our group reported some of the first examples of ketone/nitrogen-based MR-TADF emitters (**DiKTa**, aka **QAO**), the OLEDs achieved an EQE_{max} of 14.7%, with λ_{EL} of 465 nm and FWHM of 39 nm.[11,18] Numerous derivatives of **DiKTa** have since been reported, with the corresponding OLEDs achieving EQE_{max} in some examples of greater than 30%.[11,18–22] Despite these impressive advances, devices that can produce the desired pure blue emission ($CIE_x + CIE_y < 0.3$) remain rare.

Here, we present a high-performance pure blue MR-TADF emitter design strategy by fusing boron and carbonyl MR-TADF cores where the boron and nitrogen atoms are disposed *para* to each other in a B-π-N manner. By fusing the two MR-TADF emitters of **DOBNA** and **DiKTa** into a single molecule, **DOBDiKTa**, not only are the MR-TADF properties conserved, but a desired color tuning to the blue and improved RISC rates were also achieved. As shown in Figure **1**, the boron atom is embedded *para* to the nitrogen atom of **DiKTa**, thus the emission is blue-shifted to 445 nm between **DiKTa** (λ_{PL} = 451 nm) and **tBuDOBNA** (λ_{PL} = 397 nm) in toluene. The emission of 1.5 wt% doped film **DOBDiKTa** in a 1:1 mixture of 1,3-bis(N-carbazolyl)benzene:2,8-Bis(diphenyl-phosphoryl)-dibenzo[b,d]thiophene (mCP:PPT) as a co-host system is 461 nm (FWHM of 38 nm) , which is nearly identical to the emission observed

in mCP at the same doping concentration (λ_{PL} = 460 nm with FWHM of 37 nm). Compared with **DiTKa**, OLEDs using the mCP:PPT co-host with **DOBDiKTa** as the emitter show an increased EQE_{max} of 17.4% and bluer emission at λ_{EL} of 458 nm (FWHM of 38 nm) associated with improved Commission Internationale de l' Éclairage (CIE) coordinates of (0.14, 0.12).

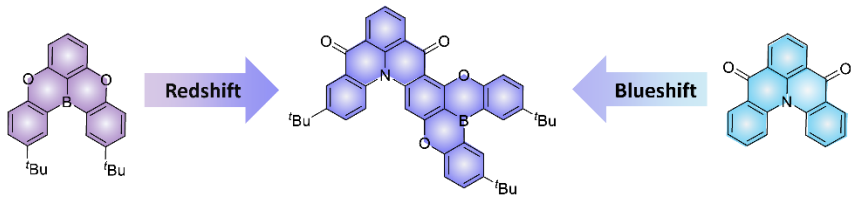

tBuDOBNA

λ_{PL}= 397 nm
FWHM = 27 nm
in toluene solution
No device

DOBDiKTa

λ_{PL} = 445 nm
FWHM = 27 nm
in toluene solution
EQE_{max} = 17.4%
CIE (0.14, 0.12)
This work

DiKTa

λ_{PL} = 451 nm
FWHM = 29 nm
in toluene solution
EQE_{max} = 14.7%
CIE (0.14, 0.18)
Adv. Opt. Mater., 2020, **8**, 1901627

Figure **1**. Comparison of the properties and structures of **tBuDOBNA**, **DOBDiKTa,** and **DiKTa**.

The molecular design for **DOBDiKTa** was rationalized through a ground- and excited-state properties computational study using a combination of gas-phase DFT (PBE0/6-31G(d,p)) and wavefunction-based (SCS-ADC(2)/cc-pVDZ) methods, respectively (Figure **2**); indeed, we have previously demonstrated DFT methods are not suitable for accurately modelling the excited states of MR-TADF compounds and so a higher level of theory is required.[23,24] From Figure **2a**, the highest occupied molecular orbitals (HOMO) is distributed over the entire π-conjugated system and the lowest unoccupied molecular orbital (LUMO) is mostly localized on the **DiKTa** fragment, similar to that calculated for **DiKTa** (Figure **S12**). The calculated HOMO and LUMO levels are -5.95 and -2.03 eV, respectively, which are destabilized compared to those of **DiKTa** (HOMO: -6.20 eV and LUMO: -2.23 eV) and stabilized compared to those of **DOBNA** (HOMO: -5.68 eV and LUMO: -1.71 eV). In the S_1 and T_1 excited states, the electron density is localized on the **DiKTa** moiety (Figure **2b**) and the corresponding difference density plots also reveal the expected alternating increasing and decreasing electron density pattern that is characteristic of excited states of short-range charge transfer (SRCT) character. The calculated S_1 and T_1 energies of **DOBDiKTa** are 3.46 and 3.27 eV, respectively, which are almost the same as those of **DiKTa** (S_1 = 3.46 eV and T_1 = 3.20 eV, Figure **S12**) and a modestly stabilized to those of **DOBANA** of (S_1 = 3.65 eV and T_1 = 3.44

eV, Figure **S13**), indicating that a similar emission energy to **DiKTa** is expected. The ΔE_{ST} of **DOBDiKTa** is 0.18 eV, which is smaller than both of **DiKTa** (0.26 eV) and **DOBNA** (0.20 eV). The oscillator strength for the S_0-S_1 transition in **DOBDiKTa** is larger at 0.30 than in both **DiKTa** (0.20) and **DOBNA** (0.17), implying a higher Φ_{PL} in the former. **DOBDiKTa** shows a small structural relaxation at the optimized singlet excited state geometry compared to the ground state geometry (Figure **S14**), which suggests that this compound should exhibit very narrowband emission. The spin-density distribution (SDD) of the T_1 state of **DOBDiKTa** is localized on the **DiKTa** fragment. The benefit of the carbonyl groups in **DOBDiKTa** is evidenced by the much large SOC matrix elements (SOCME) of 1.64 cm^{-1} compared with **DOBNA** of 0.06 cm^{-1} (SOCME of **DiKTa** is 1.83 cm^{-1}) between S_1 and T_1 (Figure **S16**). There are additionally five intermediate triplet states that lie between S_1 and T_1. The SOCME values range from 1.88 to 4.97 cm^{-1}, which are of intermediate values to those of **DiKTa** ($\langle S_1|\hat{H}_{SOC}|T_2\rangle$ = 6.32 cm^{-1}, $\langle S_1|\hat{H}_{SOC}|T_3\rangle$ = 7.77 cm^{-1}, $\langle S_1|\hat{H}_{SOC}|T_4\rangle$ = 7.59 cm^{-1}) and **DOBNA** ($\langle S_1|\hat{H}_{SOC}|T_2\rangle$ = 0.45 cm^{-1} and $\langle S_1|\hat{H}_{SOC}|T_3\rangle$ = 0.08 cm^{-1}), and point to a RISC mechanism via spin-vibronic coupling involving one or more of these states.

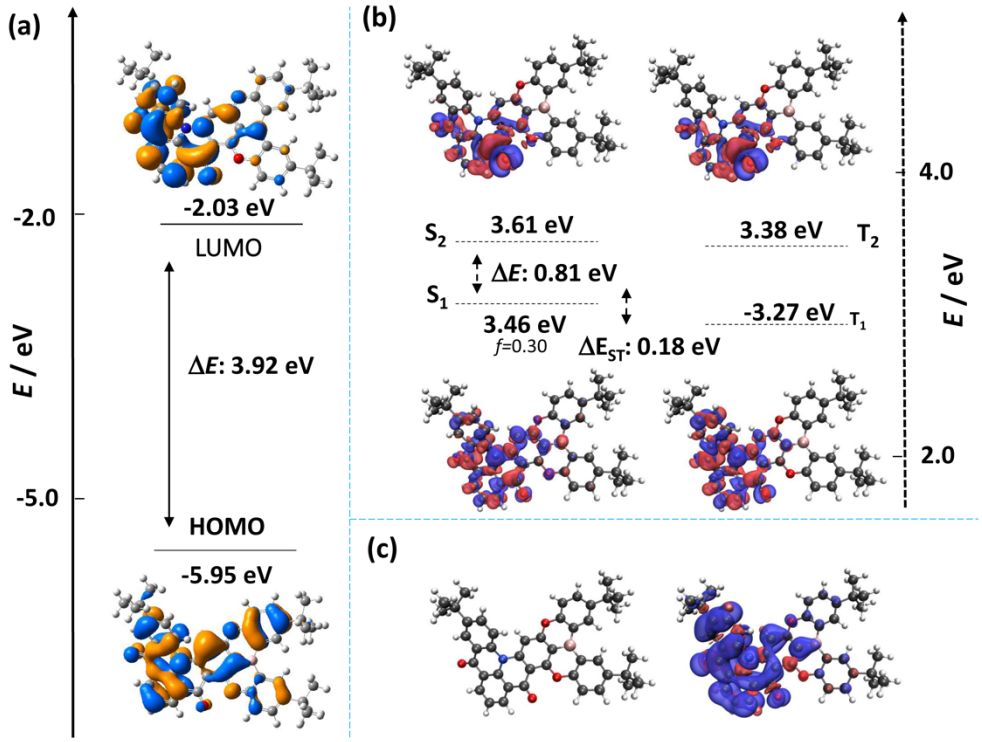

Figure **2**. a) Distributions of the frontier molecular orbitals of **DOBDiKTa**, calculated in the gas phase at the PBE0/6-31G(d,p) level. b) Difference density plots of S_1/S_2 and T_1/T_2 excited states (calculated in the gas phase at the SCS-ADC(2)/cc-pVDZ level) for **DOBDiKTa**. *f* is the oscillator strength. c) Triplet spin density of **DOBDiKTa** calculated in the gas phase at the T_1

optimized geometry at the uPBE0/6-31G(d,p) level.

The energies of the frontier molecular orbitals were inferred from the electrochemistry, measured by cyclic voltammetry (CV) and differential pulse voltammetry (DPV) in degassed DMF. The electrochemical data reported *versus* SCE are summarised in Table **S1**. As shown in Figure **S18**, there is an irreversible oxidation and a quasi-reversible reduction wave, with associated peak potentials from the DPV of 1.47 and -1.50 eV, respectively. The corresponding HOMO and LUMO levels are -5.78 and -2.80 eV, respectively, leading to an intermediate HOMO-LUMO gap of 2.98 eV compared to those **tBuBONA** (3.00 eV) and **tBuDiKTa** (2.85 eV).[25] The room temperature UV-visible absorption, steady-state photoluminescence (PL) and 77 K phosphorescence spectra of **DOBDiKTa** in dilute toluene solution are depicted in Figure **3**. The absorption spectrum possesses three distinguished peaks at 335, 374 and 429 nm (Figure **3a**). The absorption band at 300-350 nm is assigned to π-π^* transitions over the whole skeleton. The absorption band at 374 nm is assigned to the SRCT transition localized on the **tBuDOBNA** unit of **DOBDiKTa** given its similar energy to that found the absorption spectrum of **tBuDOBNA** (383 nm) as shown in Figure **S16**. The lowest energy absorption centered at 429 nm is the SRCT transition on the **DiKTa** fragment (Figure **S17**), according to the similar energy of this band to that of **DiKTa** (433 nm). Thus, though the two MR-TADF fragments of **tBuBONA** and **DiKTa** are annulated in **DOBDiKTa**, in the ground state absorption spectra, they act essentially as independent chromophores. The steady-state PL of **DOBDiKTa** in toluene evidences a narrowband blue emission, with λ_{PL} of 449 nm and a full width at half maximum (FWHM) of 26 nm. This emission is in between that of **tBuDOBNA** (397 nm) and **DiKTa** (451 nm). The mirrored absorption and emission spectra, the small Stokes shift of 20 nm (0.12 eV, shown in Figure **S20**) and small FWHM all reflect the small degree of geometric reorganization in the excited state, which is confirmed by the small configuration difference between S_1 and S_0 shown in Figure **S14**. The change in PL as a function of solvent polarity (Figure **S22**) reflects a modest positive solvatochromism that is consistent with an emissive excited state of SRCT character that is a hallmark of MR-TADF emitters. The energies of the S_1 and T_1 states were determined from the onsets of the prompt fluorescence and delayed emission in toluene glass at 77 K (Figure **3b**). The calculated S_1 and T_1 energies are 2.87 and 2.66 eV, respectively, revealing a modest ΔE_{ST} of 0.21 eV, which is in between those of **DiKTa** (0.22 eV) and **tBuDOBNA** (0.20 eV) (Figure **S21**). Steady-state and time-resolved PL in both aerated and degassed in toluene are shown in Figures **3c** and **3d**. The PL spectrum is somewhat quenched in air with the photoluminescence quantum yield, Φ_{PL}, decreasing from 48% to 29%.

The transient decays show a quenching of the delayed emission in air. The prompt and delayed lifetimes, τ_p and τ_d, are 1.9 ns and 11 µs in degassed toluene solution; the delayed emission is not detectable in aerated solution. All these results imply contributions from triplet excitons. By contrast, delayed emission was not observed in toluene solutions of **DiKTa** and **tBuDOBNA**.

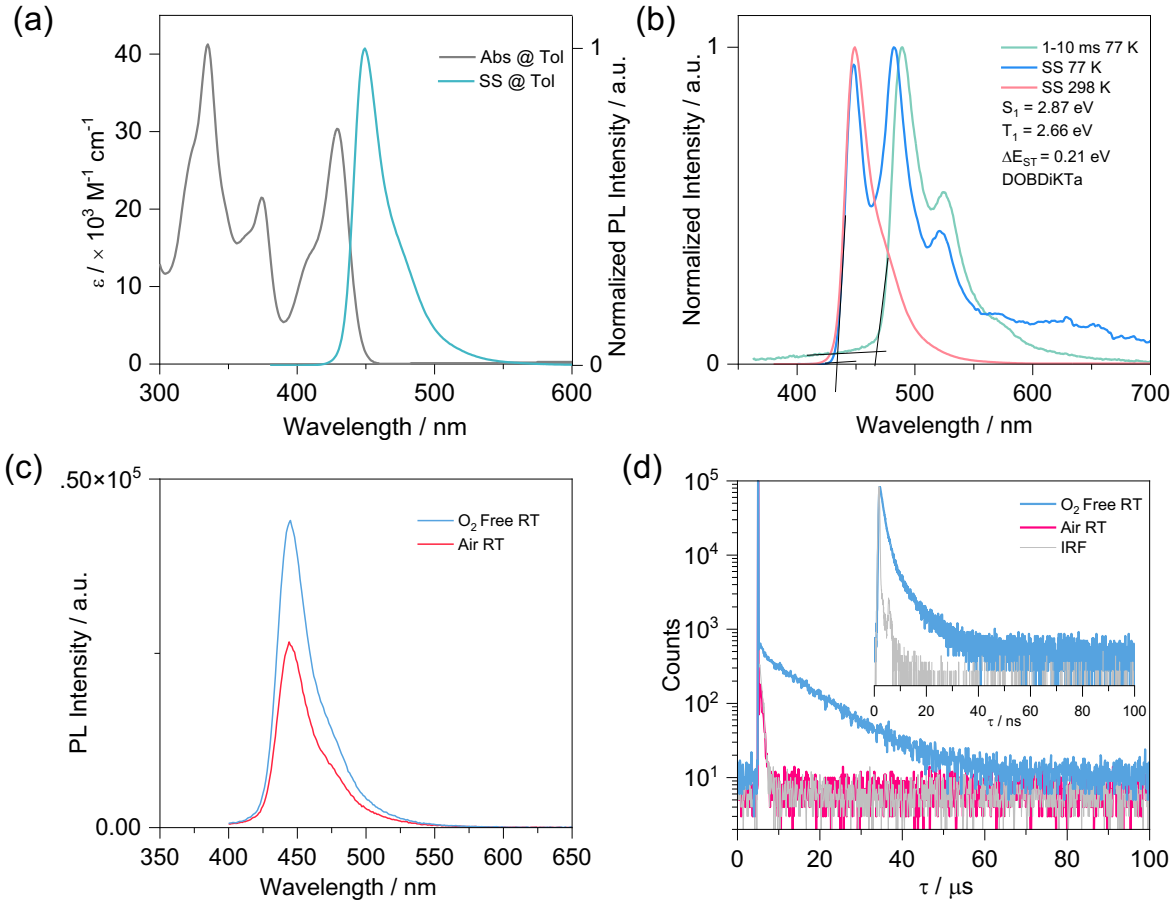

Figure **3**. (a) Absorption and steady-state PL spectra (SS) in toluene at room temperature (λ_{exc} = 340 nm); (b) prompt PL and delayed emission spectra measured in toluene glass at 77 K (λ_{exc} = 340 nm); (c) Comparison of the intensity of the PL spectra in both aerated and degassed toluene solutions (λ_{exc} = 340 nm); (d) Time-resolved PL decay (λ_{exc} = 375 nm) in toluene solution (inset figure is the PL decay of the prompt component).

Table **1**. Photophysical data of **DOBDiKTa**, **tBuDOBNA** and **DiKTa**.

Emitters	λ_{abs} nm	Φ_{PL} /%[c]	λ_{PL} /nm[d]	FWHM / nm[e]	S_1 /eV[f]	T_1 /eV[g]	ΔE_{ST}/ eV[h]	τ_p /ns[i]	τ_d

										/ μs[i]
DOB-DiKTa	sol[a]	430	48	449	26	2.79	2.64	0.15	1.9	11
	film[b]	N/A	75	460	37	2.77	2.60	0.17	2.6	43
tBuDOBNA	sol[a]	383	N/A	397	26	3.26	3.06	0.20	N/A	N/A
	film[b]	N/A	62	407	34	N/A	N/A	N/A	4.8	242
DiKTa	Sol[a]	433	N/A	451	28	2.81	2.59	0.22	N/A	N/A
	film[b]	N/A	46	467	46	N/A	N/A	N/A	9.8	-

[a] Measured in toluene solution at a concentration of 1×10^{-5} M; [b] Measured in spin-coated 1.5 wt% doped thin films in mCP. [c] the Φ_{PL} of the solution was measured using the optically dilute method and of the film was measured using an integrating sphere under nitoigen (λ_{exc} =340 nm).[26] [d] Obtained at 298 K, λ_{exc} = 340 nm. [e] Full-width at half-maximum; [f] Obtained from the onset of the SS PL spectrum at 77 K. [g] Obtained from the onset of the delayed emission spectrum (1-10 ms) at 77 K (λ_{exc} = 340 nm).[h]ΔE_{ST} = $E(S_1) - E(T_1)$. [i] Measured at 300 K under vacuum, λ_{exc} = 379 nm.

We next investigated the photophysical properties of **DOBDiKTa** in doped films in a host of suitably high triplet energy (E_{T1} = 2.81 eV), 1,3-bis(*N*-carbazolyl)benzene (mCP) as this was the host used in our prior studies of **DiKTa**.[22,27] The emission in mCP doped film red-shifts with increasing doping concentration from 1.5 to 10 wt% (Figure **S24a**), reflecting increasing contributions from aggregates to the emission. The Φ_{PL} likewise drops from 75% to 47% with increasing doping concentration (Figure **S24b**). Thus, 1.5 wt% doped film in mCP were used for the solid-state photophysical study as shown in Figure **4**. The steady-state PL shows narrowband blue emission at λ_{PL} of 460 nm with FWHM of 37 nm Figure **4a**, which is red-shift and broader compared to the spectrum in dilute toluene solution (λ_{PL}= 449 nm, FWHM= 26 nm). These spectral changes can be attributed to the presence of aggregates as well as host-guest interactions. The emission is also of intermediate wavelength to those of **DiKTa** (467 nm) and **tBuDOBNA** (407 nm), Figure **S25**. The S_1 energy was inferred from the high-energy onset of the steady-state PL at 77 K to be 2.77 eV while the T_1 energy was determined from the onset of the time-gated phosphorescence at 77 K to be 2.60 eV; thus, the ΔE_{ST} is 0.17 eV (Figure **4a**). The PL spectrum is somewhat quenched in air, with Φ_{PL} decreasing from 75% to 67%. The transient PL decay under vacuum shows biexponential kinetics with a τ_p of 2.6 ns and a τ_d of 43 μs (Figure **4b**). By contrast, **DiKTa** shows prompt and delayed lifetimes of 4.8 ns and 242 μs, while **tBuDOBNA** only shows a prompt lifetime of 9.8 ns (Figure **S27**). A rate constant analysis is summarized in Table **S2**. The singlet radiative transition rate constant (k^S_r)

of 6.0×10^7 is slower than rate constants of intersystem crossing (k_{ISC}= 2.73×10^8), which is due to the strong spin orbital coupling (SOC) induced by the carbonyl groups.[19] The rate constant for RISC, k_{RISC}, at 8.8×10^4 is almost 3.5-fold faster than that of **DiKTa** (k_{RISC}, at 2.75×10^4). The intensity of the delayed PL increases with increasing temperature, evidencing the TADF character of this compound (Figure **S26**). All these results indicate that **DOBDiKTa** has an improved TADF character compared to **DiKTa**.

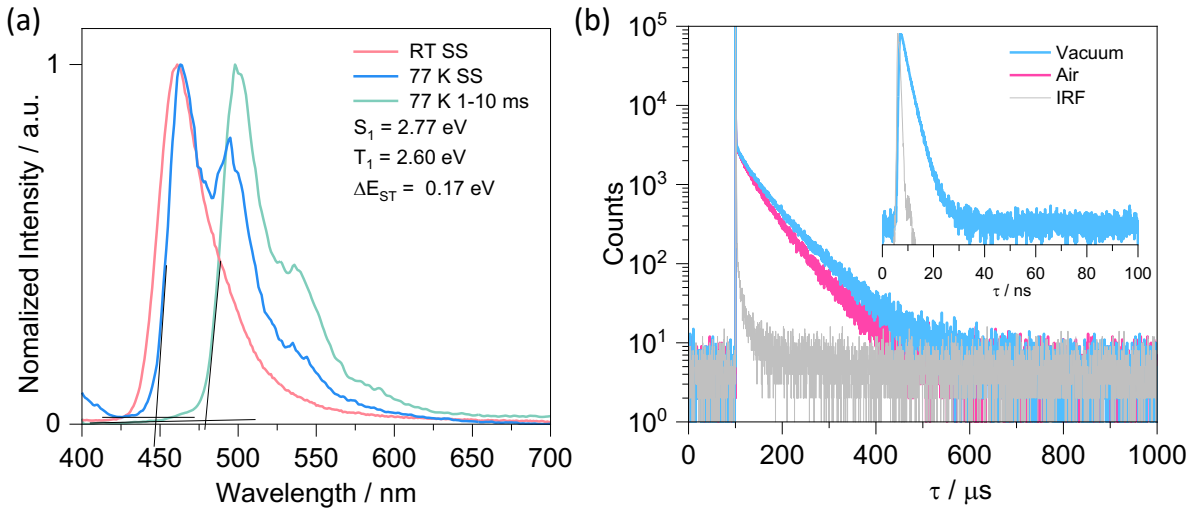

Figure **4**. (a) SSPL of **DOBDiKTa** at room temperature and at 77 K, phosphorescence spectra measured at 77 K (1-10 ms) in 1.5 wt% doped film in mCP (λ_{exc} = 340 nm); and (b) TRPL decays (λ_{exc} = 379 nm) in 1.5 wt% doped film in mCP (inset figure is the PL decay of the prompt component).

Finally, we fabricated evaporated OLEDs with the following device stack: ITO/HATCN (5 nm)/TAPC (40 nm)/TCTA (10 nm)/mCP (10 nm)/EML (20 nm)/PPT (10 nm)/TmPyPB (50 nm)/LiF (0.8 nm)/Al (100 nm), where indium tin oxide (ITO) is the anode, 1,4,5,8,9,11-hexaazatriphenylenehexacarbonitrile (HATCN) is the hole inject layer, 4,4'-cyclohexylidenebis[*N,N*-bis(4-methylphenyl)benzenamine] (TAPC) and tris(4-carbazoyl-9-ylphenyl)amine (TCTA) act as hole-transport layers, respectively. mCP is used to block excitons, 1,3,5-tri(*m*-pyridin-3- ylphenyl)benzene (TmPyPB) acts as the electron-transporting material, and LiF modifies the work function of the aluminum cathode. The device stack and the chemical structures of the materials applied in devices are shown in Figure **S30**. The device performance is summarized in Figure **5** and the data are collected in Table **2**.

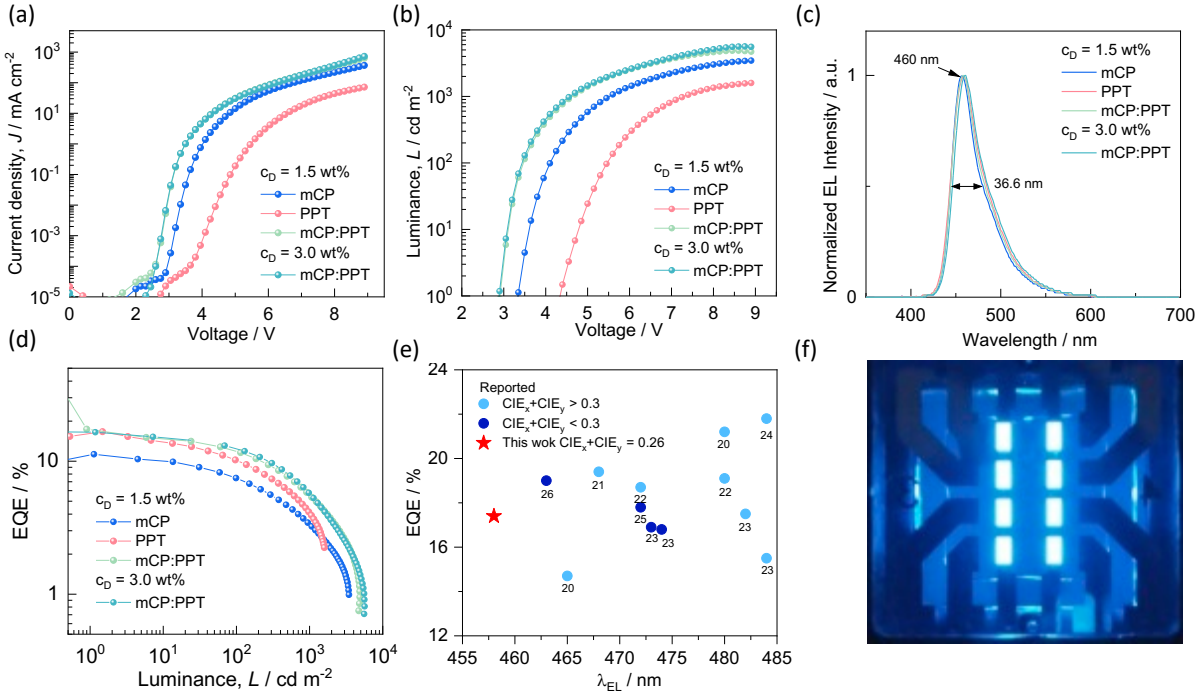

Figure **5**. (a) Current density versus voltage characteristics of the devices; (b) Luminance versus voltage characteristics for the devices; (c) Electroluminescence spectra of the devices; (d) External quantum efficiency versus luminance curves for the devices; (e) EQE_{max} of reported ketone-based MR-TADF OLEDs as a function of λ_{EL}; (f) Photograph of the devices.

Firstly, we fabricated devices using mCP as the host, device **1**. The electroluminescence (EL) spectrum shows narrowband blue emission (FWHM = 36 nm) at 457 nm (Figure **5c**), which was consistent with the thin film PL spectrum (Figure S**31**). The maximum external quantum efficiency (EQE_{max}) was 11.3% (Figure **5d**), much lower than the theoretical prediction of 15% according to EQE = IQE×η_{out}, where IQE is 75% and the light out-coupling efficiency (η_{out}) is assumed to be 20%.[28] To exclude the possible exciton loss due to the insufficient exciton confinement of the mCP host, a higher triplet energy level host, PPT [2,8-bis(diphenyl-phosphoryl)-dibenzo[b,d]thiophene, E_T = 2.96 eV] was employed.[29] The Φ_{PL} of the 1.5 wt% doped **DOBDiKTa** films in PPT increased to 79% compared to 75% in mCP at the same doping concentration. Nevertheless, the device (device **2**) with the same device structure but using PPT as the host showed EQE_{max} as high as 16.7%, which is almost a 50% improvement compared to device **1**. The significant improvement cannot be explained by the photoluminescence quantum yield alone, but instead should be related to the host material and bipolar carrier balance in the emitting layer (EML). Although a high EQE_{max} was observed in

device **2**, this device showed a 1 V larger turn-on voltage (V_{on}), lower current density, lower luminance, and larger efficiency roll-off than that of device **1 (**Figure **5**). In addition, the EL spectrum of device **2** was slightly red-shifted (λ_{EL} = 459 nm) and broadened (FWHM = 41 nm), undermining the color purity (Table **2**). The higher V_{on}, lower current density and luminance of device **2** than those of device **1** were attributed to the low carrier mobility of the electron transport type PPT host, which, however, helped enhance the recombination probability of injected electrons and holes, leading to an improved EQE at low current density. As the current density increased, the unipolar PPT host showed more severe carrier imbalance, resulting in a larger efficiency roll-off than the device with the mCP host, which is a hole-dominated bipolar host.[30] The larger permanent electronic dipole moment of PPT than mCP is responsible for the spectral red-shift and broadening.

To combine the benefits from each host, i.e., high EQE in PPT, and large luminance and good color purity in mCP, a co-host strategy was employed with a 1:1 ratio of mCP:PPT, and the same doping level of emitter (device **3**). The photophysical properties are shown in Figure **S29**, and this device shows almost the same photoluminescence with λ_{PL} at 461 nm and FWHM of 38 nm as well as similar decay kinetics with τ_p of 2.6 ns and τ_d of 60 μs. The Φ_{PL} of **DOBDiKTa** in the 1:1 co-host thin film increased to 86%. The corresponding OLED showed an improved EQE_{max} of 17.4%. Due to the bipolar character of the co-host, the V_{on} was significantly reduced from 4.3 V to 2.9 eV, a value that is similar to the emitted photon energy. In addition, the EL spectrum of device **3** was similar to that of device **1** with λ_{EL} of 458 nm and FWHM of 38 nm, resulting in a pure blue emission with CIE coordinates of (0.14, 0.12). Importantly, besides the high EQE_{max} of 17.4% and high maximum luminance (L_{max}) of 4707 cd m^{-2}, device **3** showed an improved efficiency roll-off of 32.2% at 100 cd/m^2 compared to devices **1** (34.5%) and **2** (38.9%). To further optimize the device, the doping concentration was increased to 3 wt% to improve the bipolar carrier balance (device **4**). Despite a slightly reduced EQE_{max} of 16.5%, which was attributed to the decreased Φ_{PL} of 82%, device **4** showed higher a L_{max} of 5574 cd m^{-2} and better roll-off (24.8%) at 100 cd/m^2. Device 4 arguably represent the best performing OLED of the reported carbonyl-based pure blue ($CIE_x+CIE_y < 0.3$) MR-TADF OLEDs (Table **S3** and Figure **5e**).

Table **2**. Electroluminescence data.

Device	V_{on} / V	λ_{EL} / nm	FWHM / nm	CIE (x,y)	L_{max} /cd m^{-2}	EQE $_{max/100/1000}$ / %
Device 1[a]	3.3	457	36.8	0.14,0.11	3454	11.3/7.4/3.2
Device 2[b]	4.3	459	41.4	0.14,0.12	1593	16.7/10.2/4.0
Device 3[c]	2.9	458	38.1	0.14,0.12	4707	17.4/11.8/5.5
Device 4[d]	2.9	460	39.5	0.14,0.13	5574	16.5/12.4/5.7

Emissive layer [a] 1.5 wt% **DOBDiKTa** in mCP; [b]1.5 wt% **DOBDiKTa** in PPT; [c]1.5 wt% **DOBDiKTa** in 1:1 mCP:PPT; [d] 3 wt% **DOBDiKTa** in 1:1 mCP:PPT.

In summary, we have developed a pure blue MR-TADF emitter (**DOBDiKTa**) by fusing **DiKTa** and **tBuDOBNA** together. Using this strategy, this compound emits desirably at an intermediate pure blue emission between the sky blue of **DiKTA** and the purple of **tBuDOBNA**. **DOBDiKTa** shows a high Φ_{PL} of 75%, moderate ΔE_{ST} values of 0.17 eV and shorter delayed lifetimes of 43 μs in 1.5 wt% doped mCP films. OLEDs using this emitter showed efficient performance with EQE_{max} of 11.3% with pure blue emission with λ_{EL} of 457 nm. To further optimize the device, a mixed co-host of 1:1 mCP/PPT was employed where the EQE_{max} increased from 11.3% to 17.4%, accompanied by a low V_{on} of 2.9 V and an increased L_{max} from 1600 from 5600 cd/m^2 without adversely affecting the color purity. The CIE coordinates of (0.14, 0.12) render these OLEDs as bluest device with ketone-based MR-TADF emitters.

Supporting Information

^{1}H and ^{13}C NMR spectra, HRMS and HPLC of all target compounds; supplementary computational data; supplementary photophysical data, supplementary devices data.

Acknowledgments

S.W. and JX.W. thank the China Scholarship Council (201906250199, 202006250026) for support. E.Z-C. and I.D.W.S acknowledge support from EPSRC (EP/L017008, EP/P010482/1). This paper is based on work supported in part by the Samsung Advanced Institute of Technology (SAIT).

Reference

[1] H. Uoyama, K. Goushi, K. Shizu, H. Nomura, C. Adachi, *Nature* **2012**, *492*, 234–238.
[2] C. W. Tang, S. A. Vanslyke, *Appl. Phys. Lett.,* **1987**, *51*, 913–915.
[3] M. A. Baldo, D. F. O'brien, Y. You, A. Shoustikov, S. Sibley, M. E. Thompson, S. R. Forrest, *Nature.* **1998,** 395, 151-154.
[4] M. Y. Wong, E. Zysman-Colman, *Adv. Mater.,* **2017**, *29*, 1605444.
[5] F. Dumur, D. Bertin, D. Gigmes, *Int. J. Nanotechnol.,* **2012**, *9*, 377–395.
[6] A. Niwa, T. Kobayashi, T. Nagase, K. Goushi, C. Adachi, H. Naito, *Appl. Phys. Lett.,* **2014**, *104*, 213303.
[7] P. Data, P. Pander, M. Okazaki, Y. Takeda, S. Minakata, A. P. Monkman, *Angew. Chem. Int. Ed.,* **2016**, *128*, 5833–5838.
[8] I. S. Park, M. Yang, H. Shibata, N. Amanokura, T. Yasuda, *Adv. Mater.,* **2022**, *34*, 2107951.
[9] A. C. Arsenault, D. P. Puzzo, I. Manners, G. A. Ozin, *Nat. Photonics,* **2007**, *1*, 468–472.
[10] T. Hatakeyama, K. Shiren, K. Nakajima, S. Nomura, S. Nakatsuka, K. Kinoshita, J. Ni, Y. Ono, T. Ikuta, *Adv. Mater.* **2016**, *28*, 2777–2781.
[11] D. Hall, S. M. Suresh, P. L. dos Santos, E. Duda, S. Bagnich, A. Pershin, P. Rajamalli, D. B. Cordes, A. M. Z. Slawin, D. Beljonne, A. Köhler, I. D. W. Samuel, Y. Olivier, E. Zysman-Colman, *Adv Opt. Mater.* **2020**, *8*, 1901627.
[12] Y. Kondo, K. Yoshiura, S. Kitera, H. Nishi, S. Oda, H. Gotoh, Y. Sasada, M. Yanai, T. Hatakeyama, *Nat. Photonics,* **2019**, *13*, 678–682.
[13] V. V. Patil, H. L. Lee, I. Kim, K. H. Lee, W. J. Chung, J. Kim, S. Park, H. Choi, W. J. Son, S. O. Jeon, J. Y. Lee, *Adv. Sci.,* **2021**, *8*, 2101137.
[14] H. Hirai, K. Nakajima, S. Nakatsuka, K. Shiren, J. Ni, S. Nomura, T. Ikuta, T. Hatakeyama, *Angew. Chem. Int. Ed.,* **2015**, *127*, 13785–13789.
[15] Y. Wang, L. Wang, J. Xia, Z. Lai, G. Tian, X. Zhang, Z. Hou, X. Gao, W. Mi, C. Feng, M. Zeng, G. Zhou, G. Yu, G. Wu, Y. Zhou, W. Wang, X. xiang Zhang, J. Liu, *Nat. Commun,* **2020**, *11*, 1-8.
[16] D. H. Ahn, S. W. Kim, H. Lee, I. J. Ko, D. Karthik, J. Y. Lee, J. H. Kwon, *Nat. Photonics,* **2019**, *13*, 540–546.
[17] H. Lim, H. J. Cheon, S. J. Woo, S. K. Kwon, Y. H. Kim, J. J. Kim, *Adv. Mater.,* **2020**, *32*, 2004083.
[18] Y. Yuan, X. Tang, X. Y. Du, Y. Hu, Y. J. Yu, Z. Q. Jiang, L. S. Liao, S. T. Lee, *Adv. Opt. Mater.,* **2019**, *7*, 1801536.
[19] F. Huang, K. Wang, Y. Z. Shi, X. C. Fan, X. Zhang, J. Yu, C. S. Lee, X. H. Zhang, *ACS Appl. Mater. Interfaces,* **2021**, *13*, 36089–36097.
[20] X. Qiu, G. Tian, C. Lin, Y. Pan, X. Ye, B. Wang, D. Ma, D. Hu, Y. Luo, Y. Ma, *Adv. Opt. Mater.,* **2021**, *9*, 2001845.
[21] S. Wu, A. Kumar Gupta, K. Yoshida, J. Gong, D. Hall, D. B. Cordes, A. M. Z. Slawin, I. D. W. Samuel, E. Zysman-Colman, **2022**, *Angew. Chem. Int. Ed.,* **2022**, *61*, 202213697.
[22] S. Wu, W. Li, K. Yoshida, D. Hall, S. Madayanad Suresh, T. Sayner, J. Gong, D. Beljonne, Y. Olivier, I. D. W. Samuel, E. Zysman-Colman, *ACS Appl. Mater. Interfaces,* **2022**, *14*, 22341.
[23] A. Pershin, D. Hall, V. Lemaur, J. C. Sancho-Garcia, L. Muccioli, E. Zysman-Colman, D. Beljonne, Y. Olivier, *Nat. Commun,* **2019**, *10*, 597.
[24] D. Hall, J. C. Sancho-García, A. Pershin, G. Ricci, D. Beljonne, E. Zysman-Colman, Y.

Olivier, *J Chem. Theory Comput.,* **2022**, *18*, 4903–4918.
[25] Y. J. Yu, S. N. Zou, C. C. Peng, Z. Q. Feng, Y. K. Qu, S. Y. Yang, Z. Q. Jiang, L. S. Liao, *J Mater. Chem. C,* **2022**, *10*, 4941–4946.
[26] Demasa J N, Crosby G A. *J. Chem. Phys.*, **1968**, *48*, 4726.
[27] S. A. Bagnich, A. Rudnick, P. Schroegel, P. Strohriegl and A. Köhler, Philos. *Trans. A. Math. Phys. Eng. Sci*., **2015**, *373*, 20140446.
[28] L. H. Smith, J. A. E. Wasey, W. L. Barnes, *Appl. Phys. Lett.,* **2004**, *84*, 2986–2988.
[29] S. H. Jeong, J. Y. Lee, *J Mater. Chem.* **2011**, *21*, 14604–14609.
[30] C. H. Hsiao, S. W. Liu, C. T. Chen, J. H. Lee, *Org. Electron.* **2010**, *11*, 1500–1506.

TOC